

APPENDIX A

If $\rho_j = \hat{\rho}_j + \Delta\rho_j$ ($j=1, \dots, M$), and $\psi = \psi_o + \Delta\psi$, then equation 2 can be written,

$$s_n \approx \left(\sum_{j=1}^M (\hat{\rho}_j + \Delta\rho_j) e^{i2\pi\Delta\psi t_n} \right) e^{i2\pi\psi_o t_n} e^{i2\pi\Delta\psi t_n} \quad (\text{B.1})$$

5 Dividing each side by $e^{i2\pi\psi_o t_n}$, assuming $e^{i2\pi\Delta\psi t_n} \approx 1 + i2\pi\Delta\psi t_n$, such that,

$$\hat{s}_n^R + i\hat{s}_n^I = \left(\sum_{j=1}^M (\hat{\rho}_j^R + \Delta\rho_j^R + i(\hat{\rho}_j^I + \Delta\rho_j^I)) (c_{jn} + id_{jn}) \right) (1 + i2\pi\Delta\psi t_n) \quad (\text{B.2})$$

Rearranging equation (B.2), and splitting into real,

$$\hat{s}_n^R = \hat{s}_n^R - \sum_{j=1}^M (\hat{\rho}_j^R c_{jn} - \hat{\rho}_j^I d_{jn}) = 2\pi\Delta\psi t_n \sum_{j=1}^M (-\hat{\rho}_j^R d_{jn} - \hat{\rho}_j^I c_{jn}) + \sum_{j=1}^M (\Delta\rho_j^R c_{jn} - \Delta\rho_j^I d_{jn}) \quad (\text{B.3})$$

and imaginary components,

$$10 \quad \hat{s}_n^I = \hat{s}_n^I - \sum_{j=1}^M (\hat{\rho}_j^R d_{jn} + \hat{\rho}_j^I c_{jn}) = 2\pi\Delta\psi t_n \sum_{j=1}^M (\hat{\rho}_j^R c_{jn} - \hat{\rho}_j^I d_{jn}) + \sum_{j=1}^M (\Delta\rho_j^R d_{jn} + \Delta\rho_j^I c_{jn}) \quad (\text{B.4})$$

where \hat{s}_n^R and \hat{s}_n^I are defined in equations B.3 and B.4. Arranging in matrix format for $n=1, \dots, N$

$$\hat{\mathbf{S}} \approx \mathbf{B}\mathbf{y} \quad (\text{B.5})$$

where $\hat{\mathbf{S}} = [\hat{s}_1^R \quad \hat{s}_2^R \quad \dots \quad \hat{s}_N^R \quad \hat{s}_1^I \quad \hat{s}_2^I \quad \dots \quad \hat{s}_N^I]^T$,

$$\mathbf{y} = [\Delta\psi \quad \Delta\rho_1^R \quad \Delta\rho_1^I \quad \Delta\rho_2^R \quad \Delta\rho_2^I \quad \dots \quad \Delta\rho_M^R \quad \Delta\rho_M^I]^T, \quad g_{jn}^R = 2\pi t_n \sum_{j=1}^M (-\hat{\rho}_j^R d_{jn} - \hat{\rho}_j^I c_{jn}) \text{ and}$$

15 $g_{jn}^I = 2\pi t_n \sum_{j=1}^M (\hat{\rho}_j^R c_{jn} - \hat{\rho}_j^I d_{jn})$, such that,

$$\mathbf{B} = \begin{bmatrix} g_{11}^R & c_{11} & -d_{11} & c_{21} & -d_{21} & \dots & c_{M1} & -d_{M1} \\ g_{12}^R & c_{12} & -d_{12} & c_{22} & -d_{22} & \dots & c_{M2} & -d_{M2} \\ \dots & \dots \\ g_{1N}^R & c_{1N} & -d_{1N} & c_{2N} & -d_{2N} & \dots & c_{MN} & -d_{MN} \\ g_{11}^I & d_{11} & c_{11} & d_{21} & c_{21} & \dots & d_{M1} & c_{M1} \\ g_{12}^I & d_{12} & c_{12} & d_{22} & c_{22} & \dots & d_{M2} & c_{M2} \\ \dots & \dots \\ g_{1N}^I & d_{1N} & c_{1N} & d_{2N} & c_{2N} & \dots & d_{MN} & c_{MN} \end{bmatrix} \quad (\text{B.6})$$

APPENDIX B

Multi-Coil “Dixon” Chemical Species Separation with an Iterative Least Squares Estimation Method

Scott B. Reeder, Zhifei Wen, Huanzhou Yu, Angel R. Pineda,
Garry E. Gold, Michael Markl, and Norbert J. Pelc

Submitted 7 July, 2003 to *Magnetic Resonance in Medicine* as a Full Paper,

Running title: Multi-Coil “Dixon” Chemical Species Separation

Correspondence:

Scott B. Reeder, MD, PhD
Rm H1306, Department of Radiology,
Stanford University Medical Center,
300 Pasteur Ave,
Stanford, CA, 94304
650-723-8463 (tel)
650-723-1909 (fax)
sreeder@stanford.edu

Abstract:

This work describes a new approach to multi-point “Dixon” fat-water separation that is amenable to pulse sequences that require short echo time increments, such as steady state free precession (SSFP) and fast spin echo (FSE) imaging. Using an iterative linear least squares method that decomposes water and fat images from source images acquired at short echo time increments, images with high SNR and uniform separation of water and fat are obtained. This algorithm extends to multi-coil reconstruction with minimal additional complexity. Examples of single coil and multi-coil fat-water decompositions are shown from source images acquired at both 1.5T and 3.0T. Examples in the knee, ankle, pelvis, abdomen and heart are shown, using FSE, SSFP and spoiled gradient echo pulse sequences. The algorithm was applied to systems with multiple chemical species, and an example of water-fat-silicone separation is shown. An analysis of the noise performance of this method is described and methods for improving noise performance through multi-coil acquisition and field map smoothing are discussed.

Key Words: fat suppression, musculoskeletal imaging, cardiac imaging, magnetic resonance imaging, steady-state free precession, fast spin echo, phased array coils, silicone

Introduction:

Steady-state free precession (SSFP) is a rapid, short TR imaging technique with specific advantages compared to short TR gradient echo techniques, including a high signal-to-noise ratio (SNR) and favorable contrast behavior, especially for visualizing fluid, because its contrast depends upon both T_1 and T_2 [1-3]. However, utilization of SSFP has been limited by the fact that fluid and fat both appear bright on SSFP images. This characteristic of SSFP may cause abnormalities to appear similar to normal fat and, thereby, obscure underlying pathology.

The application of “Dixon” fat-water separation method to SSFP imaging is an approach that could potentially provide homogeneous and reliable separation of fat and water from SSFP images [4, 5]. Current methods for SSFP fat suppression include fluctuating equilibrium magnetic resonance (FEMR), linear combination SSFP, and fat suppressed SSFP; however, all are sensitive to field heterogeneities [6-8]. The combination of “Dixon” methods with SSFP has been challenging for several reasons. First, SSFP requires short repetition times (TR) to prevent image degradation from field heterogeneities [1, 2], a constraint that limits TE increments to values that are smaller than those traditionally used in three point “Dixon” methods [5]. In addition, resonant frequency offsets from chemical shift and field heterogeneities produce additional phase shifts unique to SSFP that are problematic for “Dixon” fat-water decomposition techniques [2, 6].

Application of “Dixon” imaging to fast spin-echo (FSE) sequences has also been limited because the acquisition of echoes at different time shifts with respect to the spin-echo increases the spacing between successive refocusing pulses (echo spacing) [9]. Increasing the echo spacing reduces the number of echoes that can be collected in a time that maintains acceptable blurring from T_2 decay [10], offsetting the scan time benefits of FSE. A fat-water separation method that permitted shorter time increments would reduce the time between refocusing pulses and be beneficial to fast spin-echo imaging.

Dixon fat-water decomposition techniques have historically been limited to single coil acquisitions because decomposition algorithms require phase unwrapping algorithms that are problematic when multiple surface coils are involved. Fat-water decomposition with multi-coil reception in combination with phase unwrapping algorithms has been described recently [11].

In this work, we describe a new method for implementing “Dixon” fat-water separation utilizing an iterative least-squares method that reconstructs data acquired at short echo time increments, yielding images with high SNR and uniform separation of fat signal from water signal. This algorithm extends naturally to multi-coil reconstruction with minimal additional complexity and single and multi-coil decompositions derived from images obtained at both 1.5T and 3.0T are shown. Examples of fat-water separation in the knee, ankle, pelvis and heart are shown with SSFP, FSE and other pulse sequences. The algorithm is also applied to separation of multiple chemical species and examples of water-fat-silicone separation are shown. An analysis of the noise performance of this method is provided and methods for improving noise performance through field map smoothing are discussed as well as the effects of errors in presumed chemical shift are discussed.

Theory:

The application of traditional three-point “Dixon” fat-water separation to SSFP and FSE has been challenging. Three point methods described previously by Glover [5] describe the special case of phase shifts of 0, π , and 2π which correspond to echo time increments of 0, 2.2ms and 4.4ms at 1.5T and 0, 1.1ms and 2.2ms at 3T. Unfortunately, such echo time increments cause significant lengthening of the minimum TR. When using SSFP, increases in TR can lead to severe image degradation from banding artifacts caused by off-resonance field heterogeneities and chemical shift. When applied to FSE, this method increases echo spacing by 4.4ms at 1.5T, limiting the maximum echo train length in order to prevent blurring from T_2 decay, and also the number of slices per unit scan time. A recently described modified three point method that acquires images at phase shifts of 0, $\pi/2$, and π , acquiring images at 0, 1.1, 2.2ms at 1.5T has been applied to FSE and partially alleviates this problem and is restricted to a specific echo time increment [12].

An iterative linear least-squares approach was formulated and a generalized algorithm with arbitrary echo times and multiple chemical species was developed and is described below. This is followed by a description of its extension to multi-coil applications and an algorithm that summarizes our approach to decomposition of each chemical species. Finally, a noise analysis of this algorithm is provided.

Signal Model

Consider the signal in an image from a pixel containing M species each with chemical shift (Hz), Δf_j ($j=1, \dots, M$) located at position, \mathbf{r} , acquired at an echo time, t ,

$$s(t) = \left(\sum_{j=1}^M \rho_j e^{i2\pi\Delta f_j t} \right) e^{i2\pi\psi t} \quad (1)$$

where ρ_j is the intensity of the j^{th} species, and is in general, a complex term with its own magnitude, $|\rho_j|$ and phase, ϕ_j , and ψ is the local magnetic field heterogeneity (Hz). If measurements are made at discrete echo times, t_n ($n=1, \dots, N$), then,

$$s_n = \left(\sum_{j=1}^M \rho_j e^{i2\pi\Delta f_j t_n} \right) e^{i2\pi\psi t_n} \quad (2)$$

representing the signal in a pixel located at position \mathbf{r} , at echo time, t_n . For FSE, t_n is the shift from the center of the spin echo that occurs at $t_n=0$. Eq. 2 contains M complex unknowns (ρ_j , $j=1, \dots, M$) and one scalar unknown (ψ), for a total of $2M+1$ unknowns. Each image contributes a real and imaginary measurement, constituting two measurements per time point, t_n . Therefore, in general, $M+1$ or more images are required to determine the system and separate all chemical species. For example, in a system with fat and water, $M=2$, and at least three or more images are required to separate fat and water.

Least Squares Estimation of Fat and Water Images

If an initial estimate of the field map, ψ_o is known, then eq. 2 can be rewritten,

$$\hat{s}_n = s_n e^{-i2\pi\psi_o t_n} = \sum_{j=1}^M \rho_j e^{i2\pi\Delta f_j t_n} \quad (3)$$

Eq. 3 is a linear system of complex equations that can be split into real (\hat{s}_n^R) and imaginary (\hat{s}_n^I) parts,

$$\hat{s}_n = \hat{s}_n^R + i\hat{s}_n^I = \sum_{j=1}^M (\rho_j^R c_{jn} - \rho_j^I d_{jn}) + i \sum_{j=1}^M (\rho_j^R d_{jn} + \rho_j^I c_{jn}) \quad (4)$$

where ρ_j^R and ρ_j^I are the real and imaginary components of the j^{th} species, $c_{jn} = \cos(2\pi\Delta f_j t_n)$ and $d_{jn} = \sin(2\pi\Delta f_j t_n)$. Eq. 4 forms a set of linear equations that is amenable to linear least squares fitting to decompose estimates of each chemical species. A detailed description is provided in appendix A.

The initial estimate of the field map (ψ_o) is then refined further by defining error terms: $\psi = \psi_o + \Delta\psi$, $\rho_j^R = \hat{\rho}_j^R + \Delta\rho_j^R$, and $\rho_j^I = \hat{\rho}_j^I + \Delta\rho_j^I$ ($j=1, \dots, M$). Inserting these expressions into eq. 2, estimates of $\Delta\psi$, $\Delta\rho_j^R$ and $\Delta\rho_j^I$ can be calculated in the least-squares sense. Details are described in appendix B. Mathematics particular to the special case for systems that contain only water and fat are described in appendix C.

Algorithm for Single Coil Acquisitions

Using the above equations and those in the appendices, the following algorithm summarizes the method used to determine the least-squares estimates of water images and fat images for each pixel:

- Estimate the signal from each chemical species using eq. A.3 and initial guess for field map, ψ_o . A useful initial guess for ψ_o is zero (Hz)
- Calculate error to field map, $\Delta\psi$, using eq. B.7
- Recalculate $\psi = \psi_o + \Delta\psi$
- Recalculate \hat{s}_n (eqs. 3 and 4) with the new estimate of ψ
- Repeat preceding three steps until $\Delta\psi$ is small (eg. <1 Hz)
- Spatially filter (smooth) final field map, ψ , with low pass filter
- Recalculate final estimate of each chemical species images with eq. A.3

Filtering of the final field map is used to improve noise performance and is discussed below.

Multi-Coil Acquisition and Reconstruction Algorithm

A multi-coil acquisition with P elements collects P independent images, all with a different relative phase offset. By using the algorithm described above, P images of each chemical species are generated, as well as P field heterogeneity maps, which should not depend on coil-dependent phase shifts. The field maps are then combined by weighting the contribution from each coil by the square of the magnitude of the image contributed by that coil, in a manner similar to that performed for standard multi-coil image combination [13-15]. Specifically, for each pixel the combined field map is calculated as,

$$\psi_c = \frac{\sum_{p=1}^P \psi_p |s_p|^2}{\sum_{p=1}^P |s_p|^2} \quad (5)$$

Using the combined field map \hat{s}_n is recalculated with eq. 4 and new estimates of the P images of the different chemical species are calculated from eq. A.3. Finally, the P images for each chemical species are combined using a commonly used multi-coil reconstruction, previously described [13-15].

A summary of the final chemical species decomposition is provided below, accounting for multi-coil acquisitions, and smoothing of the final field map,

- For each coil
 - For each pixel
 - Estimate each chemical species assuming initial guess for field map, ψ_o , from eq. A.3
 - Calculate error to field map, $\Delta\psi$, from eq. B.7
 - Recalculate $\psi = \psi_o + \Delta\psi$
 - Recalculate \hat{s}_n (eqs. 3 and 4) with the new estimate of ψ
 - Repeat process until $\Delta\psi$ is small.
- If this is a multi-coil acquisition, combine P field maps into combined field map using eq. 5
- Spatially filter (smooth) field map with low-pass filter
- Recalculate final images for each chemical species with eq. A.3 for each coil
- For multi-coil acquisitions, combine final images for each chemical species from each coil using standard multi-coil combination techniques.

Noise Considerations

In the presence of noise with variance σ^2 , the covariance matrix of the estimate of $\hat{\mathbf{p}}$ from eq. A.3 is [16],

$$\text{cov}(\hat{\mathbf{p}}) = \sigma^2 (\mathbf{A}^T \mathbf{A})^{-1} \quad (6)$$

if it assumed that the field heterogeneity map, ψ , is known. The diagonal elements of $\text{cov}(\hat{\mathbf{p}})$ represents the Cramer-Rao bound, or lowest possible limit of the error variance of

the M^h species. In the specific case of water and fat, with equal echo time spacing of increment Δt , such that $t_n = t_0 + n\Delta t$, with $n=0,1, \dots N-1$, the variance of fat and water estimates are equal and are determined from the diagonal terms of the covariance matrix calculated from eq. 6,

$$\text{var}(\hat{\rho}) = \frac{N\sigma^2}{N^2 - \frac{\sin^2 N\theta}{\sin^2 \theta}} \quad (7)$$

where $\theta = \pi \Delta f_{fw} \Delta t$, and it has been assumed that real and imaginary parts of the signal are uncorrelated and have equal variance. As described by Glover [5], the effective number of signal averages (NSA) is,

$$NSA = \frac{\sigma^2}{\text{var}(\hat{\rho})} \quad (8)$$

and is a helpful way to describe the effect of echo time on noise behavior of a multi-point fat-water separation. Therefore, for evenly spaced echo times, the effective number of signal averages is,

$$NSA = N - \frac{1}{N} \frac{\sin^2 N\theta}{\sin^2 \theta} \quad (9)$$

representing the upper limit of effective signal averaging and noise performance for any N -point fat-water estimation technique. The optimal echo time spacing that maximizes NSA occurs when $N\theta = \pi$, such that $\Delta t = 1/N\Delta f_{fw}$, which is an intuitive result reflecting the

fact that optimal sampling should occur when the phase differences between fat and water are evenly distributed around the unit circle. At this echo spacing, $NSA=N$, demonstrating that for images acquired at the optimal echo spacing, the SNR of the calculated water and fat images is equivalent to average of N source images. Therefore, multi-point “Dixon” decomposition performed at the optimal echo time spacing is efficient from a signal to noise ratio perspective.

Figure 1a plots eq. 9 for $N=3$ and $N=4$ at 1.5T, representing the upper limits of noise performance for a multi-point fat water decomposition, assuming that the relative chemical shift of fat and water is -3.5ppm ($\Delta f_{fw} = -220$ Hz at 1.5T). For example, the optimal echo spacing at 1.5T for a three equally spaced echoes is 1.5ms, and 1.1ms for a four echo acquisition.

In the case of three species, the calculated values of NSA are not equal for each of the three species. For such a system, the NSA for each of the three species is:

$$NSA_w = N + \frac{(2ABC - N(A^2 + B^2))}{N^2 - C^2} \quad (10a)$$

$$NSA_f = N + \frac{(2ABC - N(A^2 + C^2))}{N^2 - B^2} \quad (10b)$$

$$NSA_s = N + \frac{(2ABC - N(B^2 + C^2))}{N^2 - A^2} \quad (10c)$$

where $A = \frac{\sin(\pi\Delta f_{12}N\Delta t)}{\sin(\pi\Delta f_{12}\Delta t)}$, $B = \frac{\sin(\pi\Delta f_{13}N\Delta t)}{\sin(\pi\Delta f_{13}\Delta t)}$, $C = \frac{\sin(\pi\Delta f_{23}N\Delta t)}{\sin(\pi\Delta f_{23}\Delta t)}$, and Δf_{12} , Δf_{13} , and Δf_{23} are relative chemical shifts of species 1 to 2, species 1 to 3, and species 2 to 3, respectively. Fig. 1b plots eqs. 10a-c assuming the chemical shifts of fat and silicone relative to water are -3.5ppm (-220Hz at 1.5T) and -4.9ppm (-310Hz at 1.5T), respectively [17]. From this figure, the increment in echo time that optimizes the noise performance for silicone, fat and water is approximately 2.4ms at 1.5T.

Materials and Methods:

Images of human volunteers were obtained on a 1.5T GE CV/i scanner, 1.5T GE TwinSpeed scanner and a 3.0T GE VH/i scanner. A standard extremity coil was used for imaging the knee and ankle at 1.5T, a prototype phased array multi-coil was used for the knee and ankle at 3.0T, and a standard phased array torso coil were used for imaging the heart, pelvis and abdomen at 1.5T. The study was approved by our institutional review board. Prior to imaging, informed consent was obtained from all volunteers. Product automated shim routines were used for all imaging.

3D-SSFP imaging was performed in the knee, ankle and pelvis. Typical imaging parameter for the knee and ankle included: $N_x=256$ (fractional readout), $N_y=192$, $NSA=1$, $FOV=16\text{cm}$, $\text{slice}=1.5\text{mm}$, $N_z=32-64$, $TR=5.6-6.2$, and three or four echoes spaced by approximately 1ms (1.5T) and 0.5ms (3.0T). Bandwidth at 1.5T was $\pm 125\text{kHz}$ and $\pm 42\text{kHz}$ at 3.0T. Imaging parameters in the pelvis included: $N_x=512$, $N_y=X$, $NSA=1$, $FOV=32\text{cm}$, $\text{slice}=4\text{mm}$, $N_z=32$, $TR=5.5\text{ms}$, and three echoes ($TE=0.9, 1.9, 2.9\text{ms}$).

To demonstrate the ability of the “Dixon” method to separate fat and water in the presence of a heterogeneous magnetic field, 3D spoiled gradient echo (SPGR) images with

fat saturation were obtained in the knees and ankles at both 1.5T and 3.0T. Matrix size, field of view and slice thickness were the same as SSFP images. Other parameters included: TR=50ms, TE=5ms (full echo), tip angle = 40°, and BW = $\pm 16\text{kHz}$. These parameters are based on established reports using fat saturated SPGR imaging of articular cartilage [18, 19]. Total scan time for a 64 slice FS-SPGR set of images was 12:04 min. Comparison fat-saturated FSE images were also obtained in the abdomen, with the same imaging parameters used for the “Dixon” acquisition, except that 3 signal averages were used to obtain comparable SNR.

Cardiac images were acquired at 1.5T with a modified 2D retrospectively gated SSFP sequence with the following imaging parameters: $N_x=224$ (fractional readout), $N_y=128$, NSA=1, FOV=32cm, slice=8mm, TR=5.2, and three echoes (TE=0.9, 1.9, 2.9). Twenty phases were acquired through systole and diastole with a segmentation factor of 16 for a time resolution of 83ms. Total breath-hold time for one slice was approximately 20-24s, depending on heart-rate.

FSE images were acquired in the knee and abdomen. In the knee, imaging parameters included: BW= $\pm 16\text{kHz}$, $N_x=320$, $N_y=224$, NSA=1, FOV=16cm, slice=2mm, TR=5000ms, effective TE=10ms, echo-spacing=13.6ms and three echo time increments ($\Delta\text{TE}=-1.0\text{ms}$, 0ms, 1.0ms). In the abdomen, imaging parameters included: torso phased array coil, respiratory triggering, BW= $\pm 31.3\text{kHz}$, $N_x=384$, $N_y=192$, NSA=1, $\text{FOV}_x=34\text{cm}$, $\text{FOV}_y=25.5\text{cm}$ slice=8mm, effective TE=90ms, echo-spacing=13.6ms and three echo time increments ($\Delta\text{TE}=-1\text{ms}$, 0ms, 1ms). For comparison, fat saturated FSE images were obtained with identical imaging parameters and NSA=3.

SPGR imaging of a silicone-fat-water phantom was performed at 1.5T using a standard head coil. Sylgard 527 Dielectric Silicone Gel (Dow Corning, Midland, MI) was obtained and parts A and B were mixed in a ratio of 6:7 and allowed to set in a 15cc and 50cc vial. Olive oil was placed in a 15cc and 50cc vial and all vials placed in a one liter vessel containing tap water. Imaging parameters included: BW= $\pm 31.3\text{kHz}$, $N_x=256$, $N_y=256$, NSA=4, FOV=16cm, slice=4mm, TR=34ms, TE=4.9, 7.3, 9.7, 12.1ms.

An off-line reconstruction program written in Matlab 6.0 (Mathworks, Natick, MA) was used to perform fast Fourier transform reconstruction of all images. Following reconstruction of complex (magnitude and phase) images, estimation of water images and

fat images based on the iterative least-squares algorithm described above, was performed. Smoothing of field maps was performed with a 3x3 box-car filter.

Results:

Examples of source SSFP and FSE images, as well as calculated water and calculated fat images are shown in figs. 2-7,8-10. Uniform fat-water separation was achieved in all images with relatively short acquisition times. In SSFP imaging, fluid appears bright, which is particularly helpful in musculoskeletal imaging, providing an arthrographic effect that increases the conspicuity of cartilage defects. For example, a small focal cartilage defect in the anterior tibial cartilage of the ankle is easily seen in the water image (Fig. 5).

Cardiac SSFP images demonstrate uniform fat-water separation with good spatial and temporal resolution, acquired within one breath-hold (figs. 7). Flow artifact was minimal, and excellent fat-water separation was achieved.

Uniform fat separation was seen with multi-coil SSFP and FSE imaging in pelvis and abdomen (figs. 6,10). A rim of high signal is seen anteriorly within the FSE calculated water image (fig. 10b). This was caused by a small misregistration between sequential source images that were acquired during free breathing with respiratory triggering.

Excellent separation of silicone-fat-water was also achieved in a phantom using SPGR imaging (fig. 11). Four source images with echo time increments=2.4ms were used to optimize the SNR of this decomposition, as described in eqs. 10a-c and visualized explicitly in fig. 1b.

Discussion:

In this work we have demonstrated the feasibility of using a multi-point “Dixon” chemical shift separation technique that uses multiple images acquired at arbitrary echo time increments to separate each species with a unique chemical shift. An iterative least-squares fitting algorithm was described and implemented with pulse sequences such as SSFP and FSE that benefit from short echo time increments to maintain good image quality. This allows for optimization of SNR performance as well as tradeoffs between acquisition parameters and SNR. In addition, phase-unwrapping algorithms are not necessary with this approach; such algorithms are commonly used with “Dixon” fat-water

separation techniques and add tremendously to the complexity of the reconstruction algorithm. The approach was also extended to multi-coil acquisitions with minimal increase in complexity. In vivo examples were shown in the knee, ankle, pelvis, and heart demonstrating excellent fat-water separation. In all cases, uniform separation of all chemical species was achieved with excellent image quality and high SNR. An added benefit of “Dixon” techniques over fat-suppression techniques is that the source images, as well as fat images are available and can contribute to the diagnostic value of the study.

Artifacts will result if source images are not registered with one another, as was seen in fig. 10. Registration of source images in musculoskeletal imaging was not problematic, and registration in cardiac imaging was achieved by acquiring all images within a breath-hold. In the presence of arrhythmias, misregistration of cardiac source images could occur. Imaging within the pelvis was also not problematic, although imaging within the abdomen was more difficult because of misregistration from respiratory motion. Possible solutions include reduced scan times to acquire images within a breath-hold or interleaving echoes for different source images to register data more closely.

The mathematics of this technique was generalized to include systems with multiple chemical species such as silicone/fat/water. Simultaneous separation of these three species may be helpful in the assessment of breast implant integrity, and an example of silicone/fat/water separation was demonstrated in a phantom. Prior work with traditional three-point “Dixon” imaging has exploited the fortuitous relative chemical shifts of silicone, water, and fat, permitting the separation of water and fat into one image and silicone into a second [17].

The noise analysis presented above assumed that the field map is known precisely. In general, this is not the case, and the estimate of the field map itself is calculated from source images, which contain noise. This in turn will degrade the noise performance of the final estimates of water and fat images, and a complete description of the noise performance of multi-point fat-water decomposition must reflect the fact that the field map is an unknown quantity. The effect of estimating the field map degrades the noise performance of the water and fat estimation from that described in eq. 9.

Other factors in a noise analysis must also be considered. For example, if it assumed that the field map is smoothly varying in space, then spatial smoothing of the final estimate of the field map will improve the SNR performance of the estimation algorithm.

An alternative to smoothing the calculated field map is to smooth the source images, which is an approach that has been described previously [20, 21]. In addition, the combination of separate field maps calculated in a multi-coil algorithm further improves SNR performance of field map estimation by combining multiple contributions to the local field map. The description above, summarized in the special case described in eq. 9 is very useful, however, as it acts as an upper limit for the best achievable SNR performance for the estimation of water and fat, as well as describing the effects of echo time increment. Improvements in the noise performance of the field map estimation through smoothing and multi-coil acquisitions will improve the NSA for water and fat, but cannot exceed this upper limit. A detailed mathematical description that includes the effects of field map estimation, smoothing of field maps or source images, and multi-coil acquisitions is complex and beyond the scope of this paper.

The extension of the least-squares iterative algorithm to multi-coil acquisitions was straightforward. The calculated field map for each coil is independent of local phase shifts that may differ between coils, allowing easy combination of all field maps through well-described multi-coil combination methods. This obviated the need for complex phase unwrapping algorithms applied to the multi-coil source data. Combination of field maps using multi-coil acquisitions also improves the local SNR of the field map, improving noise performance of water and fat estimation.

The use of shorter echo time increments described in this work helps to alleviate the large increases in TR with SSFP and echo spacing with FSE, that are necessary with standard [5] and modified [12] three-point “Dixon” techniques. In general, any technique that shifts echo times will increase TR and echo spacing and does limit this approach in circumstances where the TR (SSFP) and echo spacing (FSE) must be kept very short. Recent work by Ma *et al* describes a three point “Dixon” method that acquires FSE source images at different effective echo times through the use of shifted fractional echoes and a reconstruction algorithm akin to homodyne reconstruction [22, 23]. This allows acquisition of data with echoes that are sufficiently spaced to separate fat and water, with minimal increases in the echo spacing. The same approach should be effective with the work described above, although the increase in echo spacing was relatively minimal with the low bandwidths that were used, and this approach would be most beneficial in FSE applications

that use high bandwidths. Application to SSFP imaging would help maintain short TR's, preventing image degradation from banding caused by field heterogeneities.

Although fat-water separation with the method described in this work is efficient from an SNR perspective, acquisition of a minimum of three echoes can be limiting, especially in cardiac imaging where all data must be acquired within a breath-hold. There are many strategies that can be employed to reduce total acquisition time. Many of these approaches assume that the field heterogeneity map varies smoothly varying across the object, and sampling of the central portions of k-space may be adequate to estimate the field map adequately. A simple method for scan time reduction would be the acquisition of some source images with a reduced matrix size. For example, in a three-echo acquisition scheme, reduction in the number of k_y (phase-encoding) lines of one source image would permit calculation of a low resolution field heterogeneity map, while reducing total scan time. With this low-resolution field map and two full-resolution source images, estimates of water and fat images could then be made.

Additional time savings could be made with pulse sequences that acquire multiple images in a time sequence, such as cardiac CINE imaging, in which the field maps can be assumed to vary little in time [24]. Field maps that are calculated for one image could be used for fat-water separation in multiple other images, reducing the amount of required data dramatically.

The acquisition of multiple echoes within one TR, such as a multi-echo SSFP sequence [25] or gradient-echo spin-echo (GRASE) [26] could also exploit the evolving phase of spins with different chemical shifts. The mathematics of such reconstruction schemes are more complex and must consider additional phase shifts and differential time delays between echoes acquired with different gradient polarities [27].

In systems where low bandwidths are used and significant chemical shift artifact is present in the readout direction, "Dixon" imaging could potentially be used to correct for chemical shift artifact. This could be performed by decomposing the chemical species as described in this work, then each calculated image would be shifted an amount depending on the it's chemical shift and the acquisition bandwidth. Correction for distortion from susceptibility could also be performed because the field map is known. Finally the corrected images would be recombed into a corrected image free from chemical shift and

distortion in the readout direction. A similar approach using subsequent acquisition of selective water and fat images using spectral-spatial pulses has been described [28].

Conclusions:

The iterative least-squares multi-point fat-water separation method presented in this work describes a new approach that permits the use of variable echo time increments that can be exploited to optimize SNR or improve speed performance for demanding sequences such as SSFP and FSE. The approach can be used to separate systems with three distinct chemical shifts such as silicone, fat, and water, and can also be used with multi-coil imaging.

Acknowledgments: The authors would like to thank Dwight Nishimura, PhD, Kim Butts, PhD and Peter Kellman, PhD for helpful discussions, as well as Ann Shimakawa, MSE, Jean Brittain, PhD, and Reed Busse, PhD for their assistance with images acquired at 3.0T and FSE imaging at 1.5T.

Appendix A

For $n=1, \dots, N$, eq. 4 can be written in matrix format,

$$\hat{\mathbf{S}} = \mathbf{A}\mathbf{p} \quad (\text{A.1})$$

where,

$$\hat{\mathbf{S}} = \begin{bmatrix} \hat{s}_1^R & \hat{s}_2^R & \dots & \hat{s}_N^R & \hat{s}_1^I & \hat{s}_2^I & \dots & \hat{s}_N^I \end{bmatrix}^T,$$

$$\mathbf{p} = \begin{bmatrix} \rho_1^R & \rho_1^I & \rho_2^R & \rho_2^I & \dots & \rho_M^R & \rho_M^I \end{bmatrix}^T,$$

$$\mathbf{A} = \begin{bmatrix} c_{11} & -d_{11} & c_{21} & -d_{21} & \dots & c_{M1} & -d_{M1} \\ c_{12} & -d_{12} & c_{22} & -d_{22} & \dots & c_{M2} & -d_{M2} \\ \dots & \dots & \dots & \dots & \dots & \dots & \dots \\ c_{1N} & -d_{1N} & c_{2N} & -d_{2N} & \dots & c_{MN} & -d_{MN} \\ d_{11} & c_{11} & d_{21} & c_{21} & \dots & d_{M1} & c_{M1} \\ d_{12} & c_{12} & d_{22} & c_{22} & \dots & d_{M2} & c_{M2} \\ \dots & \dots & \dots & \dots & \dots & \dots & \dots \\ d_{1N} & c_{1N} & d_{2N} & c_{2N} & \dots & d_{MN} & c_{MN} \end{bmatrix} \quad (\text{A.2})$$

where rows 1 to N of matrix \mathbf{A} are used to calculate the real components of the signal, and rows $N+1$ to $2N$ are used to calculate the imaginary components of the signal.

Using a well-described least-squares fitting approach for linear systems of equations [29], it can be shown,

$$\hat{\mathbf{p}} = (\mathbf{A}^T \mathbf{A})^{-1} \mathbf{A}^T \hat{\mathbf{S}} \quad (\text{A.3})$$

where $\hat{\mathbf{p}} = \begin{bmatrix} \hat{\rho}_1^R & \hat{\rho}_1^I & \hat{\rho}_2^R & \hat{\rho}_2^I & \dots & \hat{\rho}_M^R & \hat{\rho}_M^I \end{bmatrix}^T$, determining initial *estimates* of each chemical species.

Appendix B

If $\rho_j^R = \hat{\rho}_j^R + \Delta\rho_j^R$ and $\rho_j^I = \hat{\rho}_j^I + \Delta\rho_j^I$ ($j=1, \dots, M$), and $\psi = \psi_o + \Delta\psi$, then eq. 2 can be written,

$$s_n \approx \left(\sum_{j=1}^M (\hat{\rho}_j + \Delta\rho_j) e^{i2\pi\Delta f_j t_n} \right) e^{i2\pi\psi_o t_n} e^{i2\pi\Delta\psi t_n} \quad (\text{B.1})$$

Dividing each side by $e^{i2\pi\psi_o t_n}$, and using the Taylor approximation $e^{i2\pi\Delta\psi t_n} \approx 1 + i2\pi\Delta\psi t_n$, such that,

$$\hat{s}_n^R + i\hat{s}_n^I = \left(\sum_{j=1}^M (\hat{\rho}_j^R + \Delta\rho_j^R + i(\hat{\rho}_j^I + \Delta\rho_j^I)) (c_{jn} + id_{jn}) \right) (1 + i2\pi\Delta\psi t_n) \quad (\text{B.2})$$

Rearranging eq. B.2, and splitting into real,

$$\hat{s}_n^R = \hat{s}_n^R - \sum_{j=1}^M (\hat{\rho}_j^R c_{jn} - \hat{\rho}_j^I d_{jn}) = 2\pi\Delta\psi t_n \sum_{j=1}^M (-\hat{\rho}_j^R d_{jn} - \hat{\rho}_j^I c_{jn}) + \sum_{j=1}^M \Delta\rho_j^R c_{jn} - \sum_{j=1}^M \Delta\rho_j^I d_{jn} \quad (\text{B.3})$$

and imaginary components,

$$\hat{s}_n^I = \hat{s}_n^I - \sum_{j=1}^M (\hat{\rho}_j^R d_{jn} + \hat{\rho}_j^I c_{jn}) = 2\pi\Delta\psi t_n \sum_{j=1}^M (\hat{\rho}_j^R c_{jn} - \hat{\rho}_j^I d_{jn}) + \sum_{j=1}^M (\Delta\rho_j^R d_{jn} + \Delta\rho_j^I c_{jn}) \quad (\text{B.4})$$

where \hat{s}_n^R and \hat{s}_n^I are defined in eqs. B.3 and B.4. Arranging in matrix format for $n=1, \dots, N$

$$\hat{\mathbf{S}} \approx \mathbf{By} \quad (\text{B.5})$$

where $\hat{\mathbf{S}} = \begin{bmatrix} \hat{s}_1^R & \hat{s}_2^R & \dots & \hat{s}_N^R & \hat{s}_1^I & \hat{s}_2^I & \dots & \hat{s}_N^I \end{bmatrix}^T$,

$$\mathbf{y} = \begin{bmatrix} \Delta\psi & \Delta\rho_1^R & \Delta\rho_1^I & \Delta\rho_2^R & \Delta\rho_2^I & \dots & \Delta\rho_M^R & \Delta\rho_M^I \end{bmatrix}^T, \quad g_{jn}^R = 2\pi t_n \sum_{j=1}^M (-\hat{\rho}_j^R d_{jn} - \hat{\rho}_j^I c_{jn})$$

and $g_{jn}^I = 2\pi t_n \sum_{j=1}^M (\hat{\rho}_j^R c_{jn} - \hat{\rho}_j^I d_{jn})$, such that,

$$\mathbf{B} = \begin{bmatrix} g_{11}^R & c_{11} & -d_{11} & c_{21} & -d_{21} & \dots & c_{M1} & -d_{M1} \\ g_{12}^R & c_{12} & -d_{12} & c_{22} & -d_{22} & \dots & c_{M2} & -d_{M2} \\ \dots & \dots \\ g_{1N}^R & c_{1N} & -d_{1N} & c_{2N} & -d_{2N} & \dots & c_{MN} & -d_{MN} \\ g_{11}^I & d_{11} & c_{11} & d_{21} & c_{21} & \dots & d_{M1} & c_{M1} \\ g_{12}^I & d_{12} & c_{12} & d_{22} & c_{22} & \dots & d_{M2} & c_{M2} \\ \dots & \dots \\ g_{1N}^I & d_{1N} & c_{1N} & d_{2N} & c_{2N} & \dots & d_{MN} & c_{MN} \end{bmatrix} \quad (\text{B.6})$$

For $n=1, \dots, N$, eq. B.5 is also a linear system of equations, and estimates of \mathbf{y} can be calculated [29],

$$\mathbf{y} = (\mathbf{B}^T \mathbf{B})^{-1} \mathbf{B}^T \hat{\mathbf{S}} \quad (\text{B.7})$$

which is used to determine $\Delta\psi$, $\Delta\rho_f^R$, and $\Delta\rho_f^I$.

Appendix C

In the special case of only water and fat (Δf_{fw} = relative fat-water chemical shift) and the receive/transmit frequency of the scanner is set to the water resonance, matrices \mathbf{A} and \mathbf{B} become,

$$\mathbf{A} = \begin{bmatrix} 1 & 0 & c_1^{fw} & -d_1^{fw} \\ 1 & 0 & c_2^{fw} & -d_2^{fw} \\ \dots & \dots & \dots & \dots \\ 1 & 0 & c_N^{fw} & -d_N^{fw} \\ 0 & 1 & d_1^{fw} & c_1^{fw} \\ 0 & 1 & d_2^{fw} & c_2^{fw} \\ \dots & \dots & \dots & \dots \\ 0 & 1 & d_N^{fw} & c_N^{fw} \end{bmatrix}$$

and

$$\mathbf{B} = \begin{bmatrix} g_1^R & 1 & 0 & c_1^{fw} & -d_1^{fw} \\ g_2^R & 1 & 0 & c_2^{fw} & -d_2^{fw} \\ \dots & \dots & \dots & \dots & \dots \\ g_N^R & 1 & 0 & c_N^{fw} & -d_N^{fw} \\ g_1^I & 0 & 1 & d_1^{fw} & c_1^{fw} \\ g_2^I & 0 & 1 & d_2^{fw} & c_2^{fw} \\ \dots & \dots & \dots & \dots & \dots \\ g_N^I & 0 & 1 & d_N^{fw} & c_N^{fw} \end{bmatrix} \quad \text{C.1}$$

where $c_n^{fw} = \cos(2\pi\Delta f_{fw}t_n)$, $d_n^{fw} = \sin(2\pi\Delta f_{fw}t_n)$, $g_n^R = 2\pi t_n(-\hat{\rho}_w^I - \hat{\rho}_f^R d_n - \hat{\rho}_f^I c_n)$ and $g_n^I = 2\pi t_n(\hat{\rho}_w^R + \hat{\rho}_f^R c_n - \hat{\rho}_f^I d_n)$ are the matrix elements.

Figures:

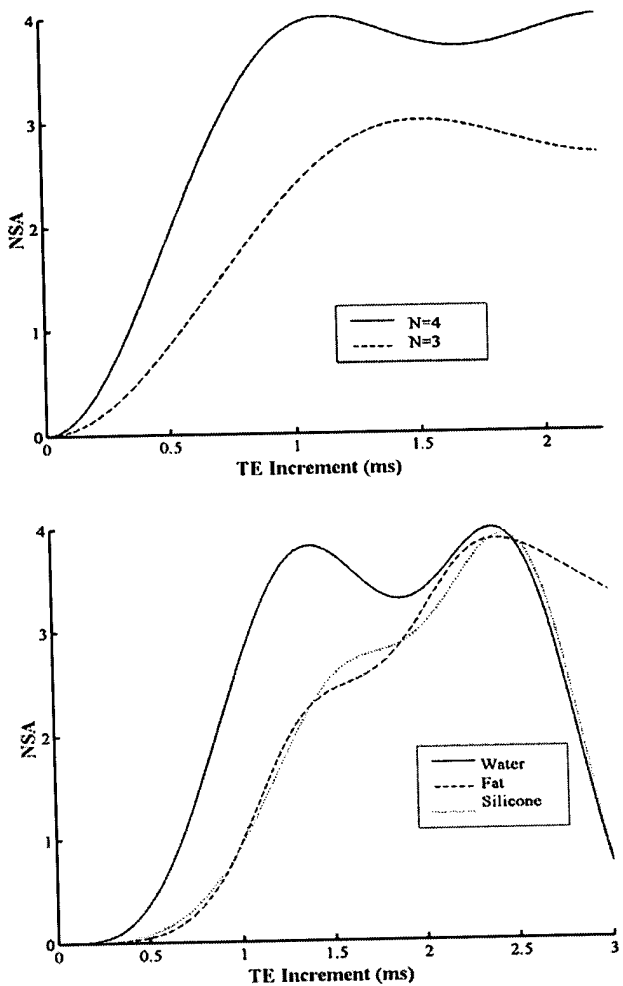


Figure 1: a) Dependence of effective number of signal averages (NSA) on echo time increment (ms) from fat-water chemical shift for three-echo (solid) and four-echo (dashed) increment (ms) from fat-water chemical shift for three-echo (solid) and four-echo (dashed) acquisition to resolve all three species at 1.5T. b) NSA for water, fat, and silicone for a four-echo acquisition to resolve all three species at 1.5T.

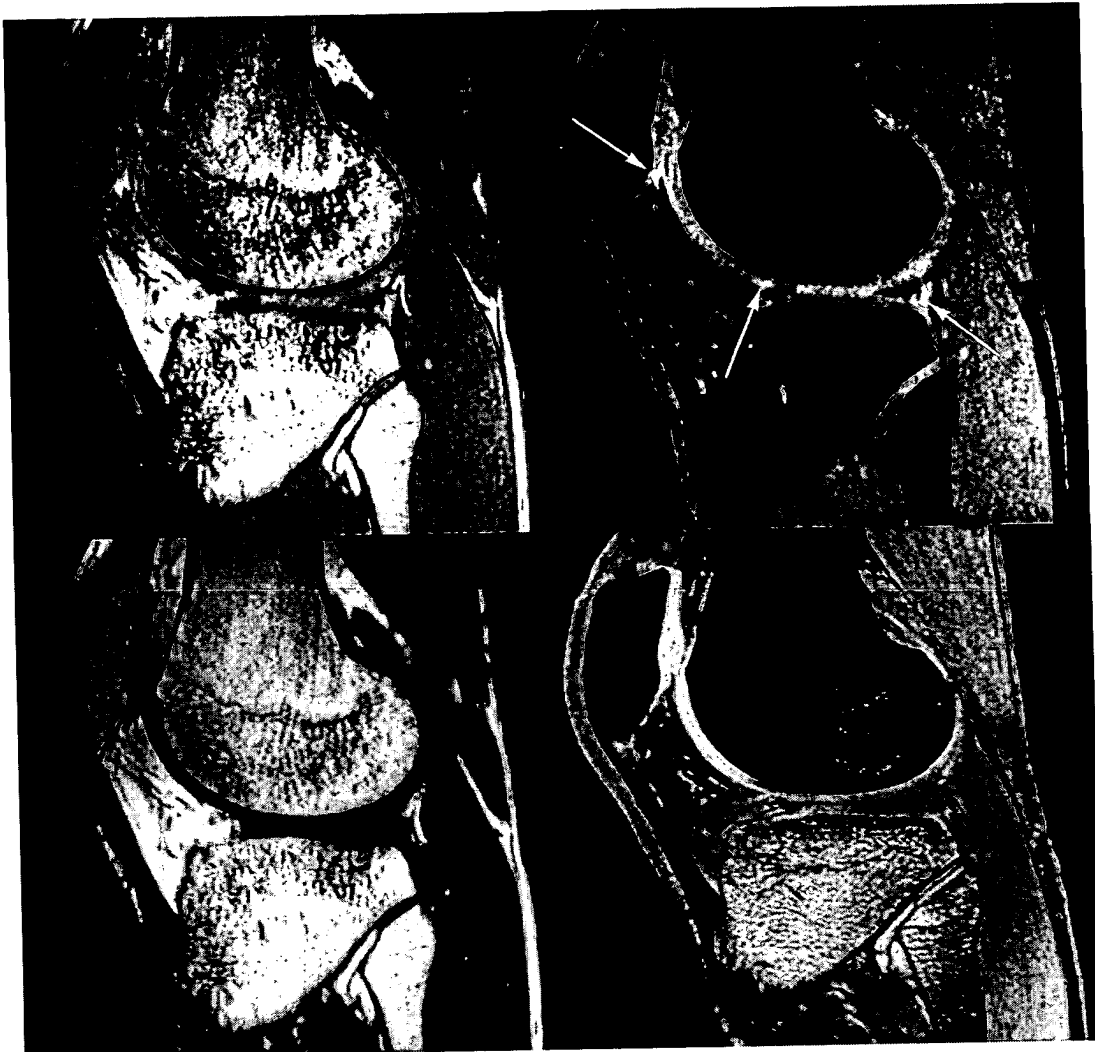


Figure 2: Sagittal SSFP images obtained in the knee of a human volunteer at 1.5T. Source (a), calculated water (b), calculated fat (c) images are shown in comparison to a fat-saturated SPGR image (d). Excellent fat-water suppression was obtained with the SSFP images, and joint fluid appears bright (arrows), providing an arthrographic effect potentially improving the conspicuity of cartilage defects. Four source images ($TE=1.2, 2.1, 3.0, 3.9\text{ms}$) were acquired and $TR=6.1\text{ms}$. Image matrix size was $256 \times 192 \times 64$, and bandwidth was $\pm 125\text{kHz}$.



Figure 3: Sagittal SSFP images obtained in the ankle of a human volunteer at 3.0T. Source (a), calculated water (b), calculated fat (c) images are shown in comparison to a fat-saturated SPGR image (d). Compared to FS-SPGR images, excellent fat-water suppression was obtained with the SSFP images, and joint fluid appears bright. Three source images were acquired ($TE=1.4, 1.9, 2.4\text{ms}$) and $TR=5.6$. Image matrix size was $256\times 192\times 32$, and bandwidth was $\pm 42\text{kHz}$.



Figure 4: Sagittal SSFP images of the knee of a human volunteer at 3.0T with a) source, b) calculated water, and c) calculated fat images. Uniform fat-water separation is identified and joint fluid appears bright. Three source images were acquired ($TE=1.4, 1.9, 2.4\text{ms}$), and $TR=5.6\text{ms}$. Image matrix size was $256\times 192\times 32$, and bandwidth was $\pm 42\text{kHz}$.



Figure 5: Sagittal SSFP images of an ankle at 1.5T with a) source, b) calculated water, and c) calculated fat images. Uniform fat-water separation is identified and joint fluid appears bright. A small defect in anterior tibial cartilage (arrow) is seen and well delineated by joint fluid which appears bright. Four source images were acquired ($TE=1.2, 2.1, 3.0, 3.9\text{ms}$), and $TR=6.1\text{ms}$. Image matrix size was $256 \times 192 \times 64$, and bandwidth was $\pm 125\text{kHz}$.

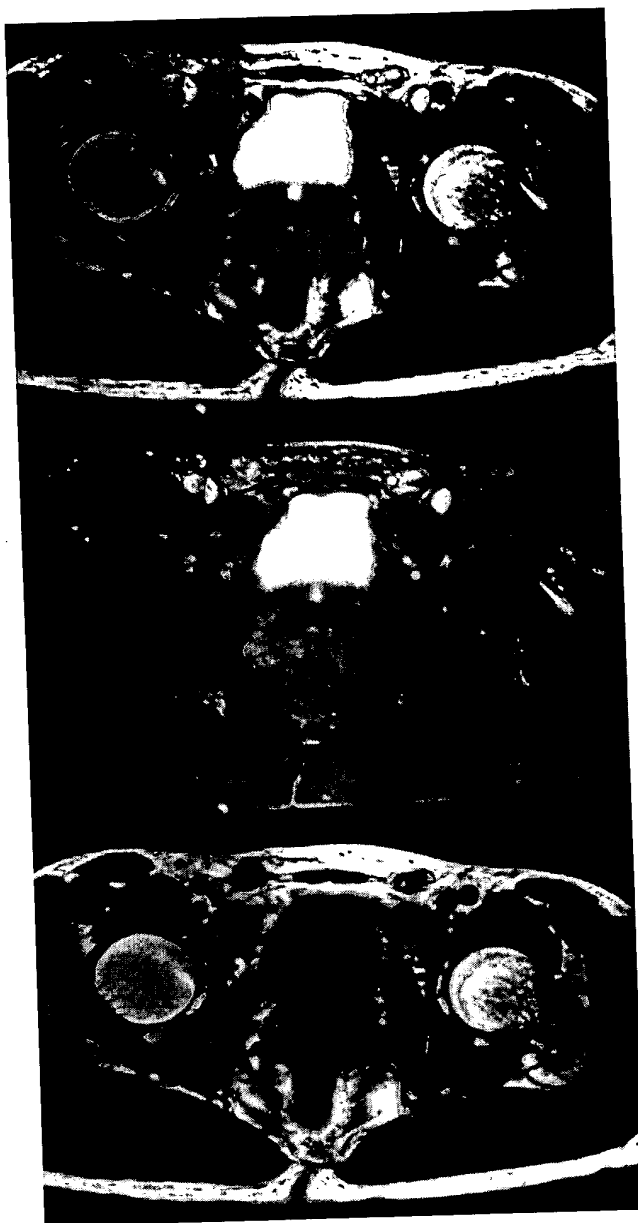


Figure 6: Axial SSFP images obtained in the pelvis of a human volunteer at 1.5T. Source (a), calculated water (b), and calculated fat (c) images demonstrate uniform fat-water separation and good image quality. Three source images were acquired ($TE=0.8, 1.8, 2.8\text{ms}$) and $TR=5.4\text{ms}$. Image matrix size was $512 \times 256 \times 32$, and bandwidth was $\pm 125\text{kHz}$.



Figure 7: Short axis CINE SSFP cardiac images acquired with torso phased array coil. Source image (left), calculated water image (middle) and calculated fat image (right) are shown at one (of 20) end diastolic phase. Uniform fat-water separation was consistently achieved in all slices and phases. Three source images were acquired ($TE=0.9, 1.9, 2.9\text{ms}$) and $TR=5.2\text{ms}$. Image matrix size was 224×128 , and bandwidth was $\pm 125\text{kHz}$.



Figure 8: Sagittal proton density FSE images of a knee of a human volunteer acquired at 1.5T with a) source, b) calculated water, and c) calculated fat images. Uniform fat-water separation is achieved and joint fluid appears bright. Three source images were acquired (shift in TE = -1.0, 0, 1.0ms), and TR=5000ms. Effective TE was 10ms and image matrix size is 320x224. Echo spacing was 13.7ms, and bandwidth was $\pm 20.8\text{kHz}$.

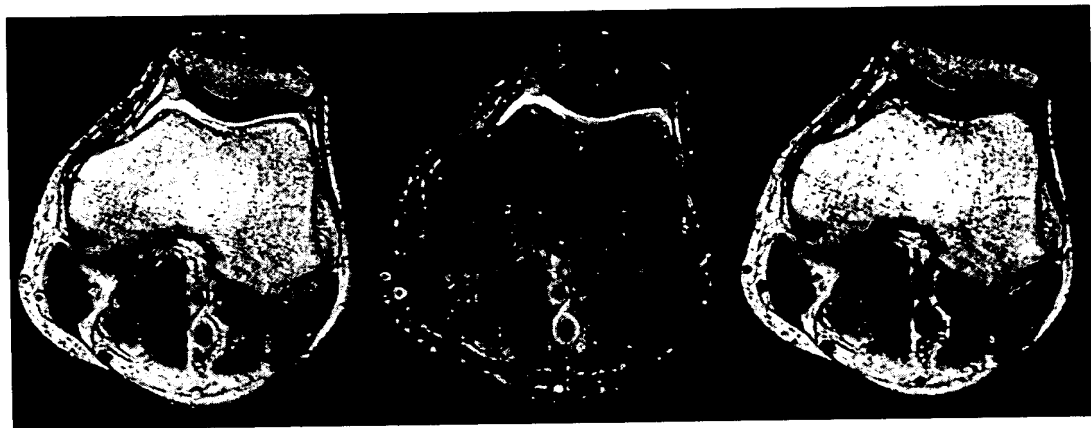


Figure 9: Axial T₂-weighted density FSE images of a knee of a human volunteer acquired at 1.5T with a) source, b) calculated water, and c) calculated fat images. Uniform fat-water separation is achieved and joint fluid appears bright. Three source images were acquired (shift in TE = -1.0, 0, 1.0ms), and TR=5000ms. Effective TE was 70ms and image matrix size is 384x192. Echo spacing was 17.5ms, and bandwidth was ± 15.6 kHz.



Figure 10: Axial T₂-weighted fast spin-echo images obtained from the abdomen of a human volunteer at the level of the spleen at 1.5 with a) source, b) calculated water, c) calculated fat images. Images were acquired with the torso phased array coil during free breathing using respiratory triggering. Uniform fat-water separation was achieved everywhere except at the anterior skin surface where misregistration between subsequent scans caused calculation errors (arrows). Three source images were acquired (shift in TE=-1.0,0,1.0ms). Effective TE was 90ms, and image matrix is 384x192 with a $\frac{3}{4}$ FOV. Echo spacing was 11.9ms and bandwidth was ± 31.3 kHz. Fat-saturated T₂-weighted fast spin-echo image with the same imaging parameters and NSA=3 is also shown (d).

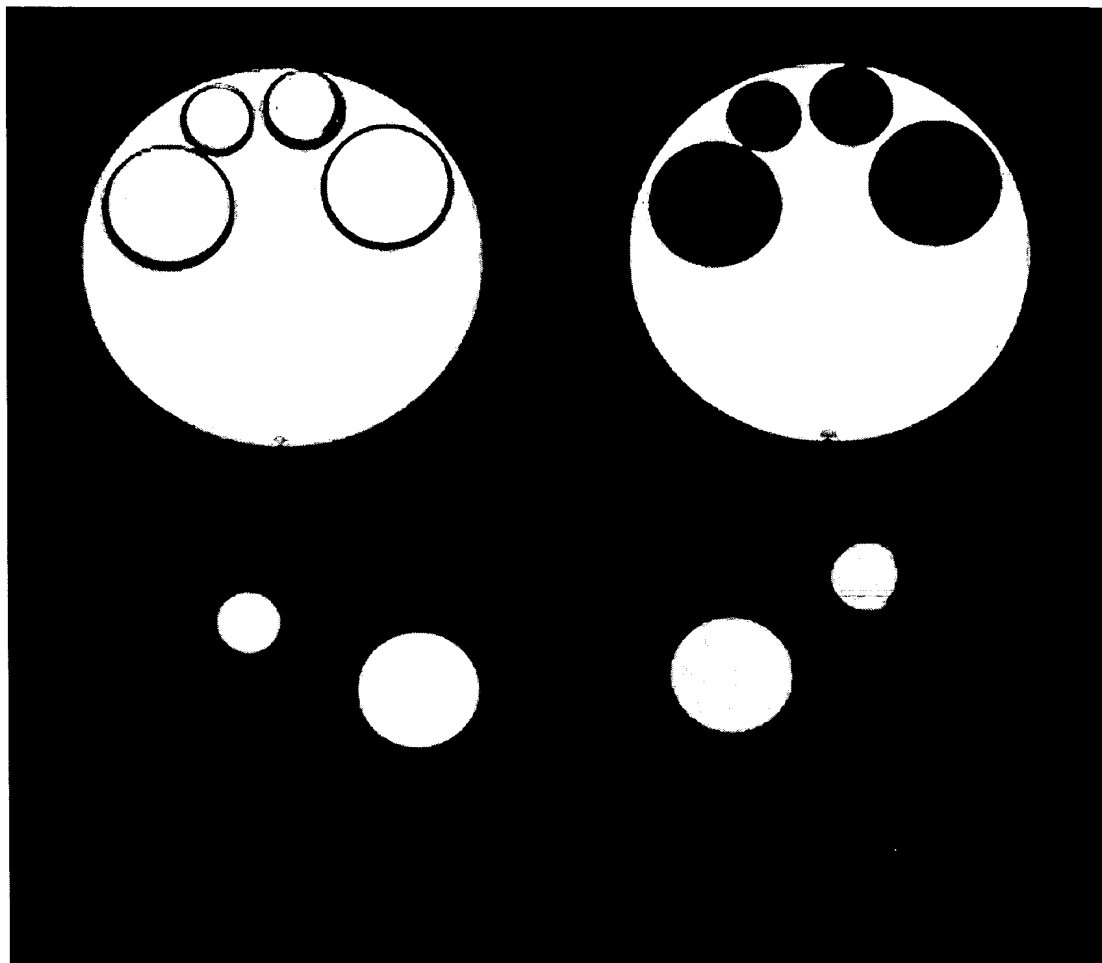


Figure 11: SPGR a) source, b) calculated water, c) calculated fat, d) calculated silicone images in a phantom. Four images were acquired (TE=4.9, 7.3, 9.7, 12.1ms) and TR=34ms. Other parameters included: 10° flip angle, 256x256 matrix, 16cm field of view, ± 31.3 kHz bandwidth, and 4mm slice thickness.

References:

1. Oppelt A. FISP. A new fast MRI Sequence. *Electromedia* **1986**;3:15-18
2. Sekihara K. Steady-state magnetizations in rapid NMR imaging using small flip angles and short repetition intervals. *IEEE Transactions in Medical Imaging* **1987**;6:157-164
3. Haacke E, Wielopolski P, Tkach J, Modic M. Steady-state free precession imaging in the presence of motion: application for improved visualization of the cerebrospinal fluid. *Radiology* **1990**;175:545-552
4. Dixon W. Simple proton spectroscopic imaging. *Radiology* **1984**;153:189-194
5. Glover G. Multipoint Dixon technique for water and fat proton and susceptibility imaging. *Journal of Magnetic Resonance Imaging* **1991**;1:521-530
6. Vasanawala SS, Pauly JM, Nishimura DG. Fluctuating equilibrium MRI. *Magn Reson Med* **1999**;42:876-883.
7. Vasanawala SS, Pauly JM, Nishimura DG. Linear combination steady-state free precession MRI. *Magn Reson Med* **2000**;43:82-90.
8. Scheffler K, Heid O, Hennig J. Magnetization preparation during the steady state: fat-saturated 3D TrueFISP. *Magn Reson Med* **2001**;45:1075-1080
9. Hardy PA, Hinks RS, Tkach JA. Separation of fat and water in fast spin-echo MR imaging with the three-point Dixon technique. *J Magn Reson Imaging* **1995**;5:181-185
10. Farzaneh F, Riederer SJ, Pelc NJ. Analysis of T2 limitations and off-resonance effects on spatial resolution and artifacts in echo-planar imaging. *Magn Reson Med* **1990**;14:123-139
11. Ma J, Singh S, Kumar A, Leeds N, Broemeling L. Phased Array Coil Compatible T2-weighted Fast Spin Echo Dixon Imaging. In: *International Society of Magnetic Resonance in Medicine*. Honolulu, HI, **2002**:735
12. Rybicki FJ, Mulkern RV, Robertson RL, Robson CD, Chung T, Ma J. Fast three-point Dixon MR imaging of the retrobulbar space with low-resolution images for phase correction: comparison with fast spin-echo inversion recovery imaging. *AJNR Am J Neuroradiol* **2001**;22:1798-1802
13. Roemer P, Edelstein W, Hayes C, Souza S, Mueller O. The NMR Phased Array. *Magn Reson Med* **1990**;16:192-225
14. Hayes C, Roemer P. Noise Correlations in Data Simultaneously Acquired from Multiple Surface Coil Arrays. *Magn Reson Med* **1990**;16:181-191
15. Bernstein M, Grgic M, Brosnan T, Pelc N. Reconstructions of Phase Contrast, Phased Array Multicoil Data. *Magn Reson Med* **1994**;32:330-334
16. Kay S. *Fundamentals of Statistical Signal Processing: Estimation Theory*. Upper Saddle River, NJ,: Prentice Hall, **1993**:83-86
17. Schneider E, Chan TW. Selective MR imaging of silicone with the three-point Dixon technique. *Radiology* **1993**;187:89-93
18. Disler DG. Fat-suppressed three-dimensional spoiled gradient-recalled MR imaging: assessment of articular and physeal hyaline cartilage. *AJR Am J Roentgenol* **1997**;169:1117-1123
19. McCauley TR, Disler DG. MR imaging of articular cartilage. *Radiology* **1998**;209:629-640
20. Rybicki FJ, Chung T, Reid J, Jaramillo D, Mulkern RV, Ma J. Fast three-point dixon MR imaging using low-resolution images for phase correction: a comparison

with chemical shift selective fat suppression for pediatric musculoskeletal imaging. *AJR Am J Roentgenol* 2001;177:1019-1023

- 21. Reeder SB, Pelc NJ, Alley MT, Gold GE. Rapid MR imaging of articular cartilage with steady-state free precession and multipoint fat-water separation. *AJR Am J Roentgenol* 2003;180:357-362
- 22. Ma J, Singh SK, Kumar AJ, Leeds NE, Broemeling LD. Method for efficient fast spin echo Dixon imaging. *Magn Reson Med* 2002;48:1021-1027
- 23. Noll DC, Nishimura DG, Macovski A. Homodyne detection in magnetic resonance imaging. *IEEE Transactions on Medical Imaging* 1991;10(2):154-163
- 24. Reeder SB, Faranesh AZ, Boxerman JL, McVeigh ER. In vivo measurement of T*² and field inhomogeneity maps in the human heart at 1.5 T. *Magn Reson Med* 1998;39:988-998
- 25. Herzka DA, Kellman P, Aletras AH, Guttman MA, McVeigh ER. Multishot EPI-SSFP in the heart. *Magn Reson Med* 2002;47:655-664
- 26. Oshio K, Feinberg DA. GRASE (Gradient- and spin-echo) imaging: a novel fast MRI technique. *Magn Reson Med* 1991;20:344-349
- 27. Bruder H, Fischer H, Reinfelder HE, Schmitt F. Image reconstruction for echo planar imaging with nonequidistant k-space sampling. *Magn Reson Med* 1992;23:311-323
- 28. Kwok WE, Totterman SM, Zhong J. 3D interleaved water and fat image acquisition with chemical-shift correction. *Magn Reson Med* 2000;44:322-330
- 29. Chapra S, Canale R. *Numerical Methods for Engineers*, 4 ed. Boston: McGraw-Hill, 2002